

LiV₂O₄: Hund-Assisted Orbital-Selective Mottness

M. Grundner ^{1,2} F. B. Kugler ³ O. Parcollet ^{3,4} U. Schollwöck ^{1,2} A. Georges ^{5,3,6,7} and A. Hampel ^{3,*}

¹*Department of Physics and Arnold Sommerfeld Center for Theoretical Physics (ASC), Ludwig-Maximilians-Universität München, D-80333 Munich, Germany*

²*Munich Center for Quantum Science and Technology (MCQST), D-80799 München, Germany*

³*Center for Computational Quantum Physics, Flatiron Institute, 162 5th Avenue, New York, NY 10010, USA*

⁴*Université Paris-Saclay, CNRS, CEA, Institut de Physique Théorique, 91191, Gif-sur-Yvette, France*

⁵*Collège de France, 11 Place Marcelin Berthelot, 75005 Paris, France*

⁶*CPHT, CNRS, Ecole Polytechnique, IP Paris, F-91128 Palaiseau, France*

⁷*DQMP, University of Geneva, 24 quai Ernest-Ansermet, 1211 Geneva, Switzerland*

(Dated: September 27, 2024)

We show that the remarkably small Fermi-liquid coherence scale and large effective mass observed in LiV₂O₄ are due to the proximity of a Hund-assisted orbital-selective Mott state. Our work is based on an ab initio dynamical mean-field approach, combining several quantum impurity solvers to capture the physics from high to very low temperature. We find that the Hund coupling plays a crucial role in rearranging the orbital populations and in generating the heavy mass and low coherence scale. The latter is found to be approximately 1–2 Kelvin, even though the most correlated orbital is found to be significantly doped ($\sim 10\%$) away from half-filling. A flat quasiparticle band appears near the Fermi level as a result of the strong electronic correlations. Finally, we discuss our results in comparison to experiments.

The ‘heavy fermion’ (HF) phenomenon – quasiparticles acquiring very large effective masses – is one of the most spectacular manifestations of strong electronic correlations. It is usually observed in materials having conduction electrons hybridizing with very localized degrees of freedom, typically *f*-orbitals in rare-earth or actinide compounds. In this context, the discovery of a remarkably large specific-heat enhancement in LiV₂O₄ (LVO), a transition-metal oxide involving no *f*-electrons, came as quite a surprise [1–3]. Indeed, only few other transition-metal compounds displaying very large mass enhancements are known to this day [4, 5].

The electronic structure of this material obtained with the density functional theory (DFT) displays two sets of bands close to the Fermi level as shown in Fig. 1 [7, 8]: one set of *a*_{1g} character, with a narrow bandwidth (~ 0.7 eV), and one set of *e*_g^π character with a broader bandwidth (~ 1.9 eV). A connection to HF materials was therefore suggested in early works [8–11], with the *a*_{1g} (resp. *e*_g^π) band playing the role of localized states (resp. conduction electrons). It was later realized, though, that this picture is not tenable. From a theoretical viewpoint, the narrow band is too broad to play the role of localized states, and, importantly, the coupling between the narrow and wide band is dominantly an intra-atomic Hund coupling which favors spin alignment, not an antiferromagnetic Kondo exchange [12–14]. Furthermore, some experimental features are markedly different from conventional HFs. The onset of Kondo coherence in HFs is typically signaled by a coherence peak in the temperature (*T*) dependence of the resistivity, followed by a lower scale *T*_{FL} below which $\sim T^2$ Fermi-liquid (FL) behavior holds. While a small FL scale *T*_{FL} ~ 2 K is indeed observed in LVO, the resistivity, however, monotonously increases upon heating, eventually reaching a ‘bad metal’

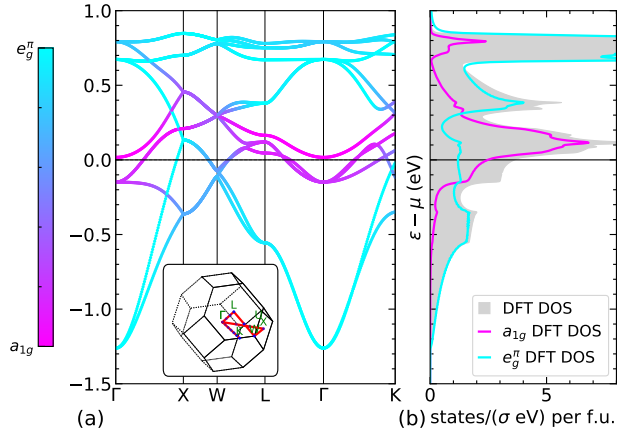


FIG. 1. (a) DFT band structure of LVO for the four *a*_{1g}- and eight *e*_g^π-like bands around the Fermi level. The eigenvalues of the MLWFs perfectly match the DFT bands [6]. Color: orbital character. Inset: Brillouin zone with high-symmetry points. (b) DFT DOS and projections onto the MLWFs.

regime at high *T* [2, 3, 15]. From various experimental probes, the onset temperature of electronic coherence is estimated as *T*_{onset} ~ 10 –30 K [2, 3, 16].

Aware of the difficulties of the Kondo scenario, Arita et al. proposed an alternative explanation [12]. In their picture, all the action takes place in the narrow *a*_{1g} band, which is viewed as a doped Mott insulator, while the broader *e*_g^π bands are merely spectators. In this description, a tiny hole doping ($\sim 2\%$) of the *a*_{1g} band yields the observed large effective mass. In support of this picture, the authors of Ref. [12] performed dynamical mean-field theory (DMFT) [17] calculations on a simplified two-orbital model down to room tempera-

ture (as well as projective Monte Carlo calculations at $T=0$). However, because of the very low energy scales involved, a full calculation of a realistic model for LVO in the DFT+DMFT framework covering the whole T range from above T_{onset} to below T_{FL} has not been achieved yet [18].

In this Letter, we leverage on recent advances in DMFT impurity solvers to achieve this goal and elucidate the physics responsible for the HF behaviour in LVO. To probe the full crossover from a higher- T incoherent metal to the low- T heavy-mass FL and to access the low FL scale, we use a combination of three DMFT solvers: Quantum Monte Carlo (QMC) for $10 \text{ K} < T < 300 \text{ K}$, tensor networks (TN) for $T > 1 \text{ K}$ and the numerical renormalization group (NRG) for $T < 1 \text{ K}$.

We show that LVO is close to a *Hund-assisted orbital-selective Mott state* [5, 14, 19–21]. The inter-orbital Hund coupling J (and therefore the e_g^π bands) plays a central role. First, it induces a redistribution of the (a_{1g} , e_g^π) orbital populations per vanadium due to interaction from $(0.4, 2 \times 0.55)$ in DFT to $(0.9, 2 \times 0.3)$ in DMFT. Second, it is responsible for the heavy mass and low T_{FL} via the spin-blocking mechanism characteristic of Hund systems in which electrons can only hop between atomic configurations with maximum spin [22–25]. LVO is shown to be close to an orbital-selective Mott state in which the a_{1g} orbital is prevented to fully localize at $T=0$ due to inter-orbital hopping [26]. Remarkably, we obtain a low T_{FL} already at $\sim 10\%$ doping of the a_{1g} band, in contrast to the $\sim 2\%$ doping of Ref. [12].

Electronic structure and effective model—LVO crystallizes in the fcc spinel structure (space group Fd3m). Crystal structure data from neutron scattering are available down to 12 K [1]. The primitive unit cell contains 14 atoms, with 4 V atoms, each embedded in an octahedral crystal field of the surrounding oxygen atoms. The octahedra themselves are corner-sharing and the local point group is trigonal D_{3d} , lowering the symmetry of the system and splitting the t_{2g} states into a single a_{1g} and a doubly degenerate e_g^π orbital higher in energy.

We perform DFT calculations using the QUANTUM ESPRESSO software package fixing the structural parameters to the 12 K experimental values [1]. Maximally localized Wannier functions (MLWFs) for the a_{1g} and e_g^π states are constructed with WANNIER90 [27], accurately reproducing the DFT low-energy electronic structure. In Fig. 1(a), the bandstructure of the Wannier Hamiltonian is shown together with its projection on the a_{1g} and e_g^π states. The projected density of states (DOS) in Fig. 1(b) reveals that the a_{1g} DOS is sharply peaked at 0.1 eV above the Fermi level, whereas the e_g^π DOS is relatively flat.

The constrained random phase approximation [28] as implemented in the RESPACK code [29] is used to determine the effective Coulomb interaction at low energy. We focus on the static, $\omega=0$ limit and fit the resulting

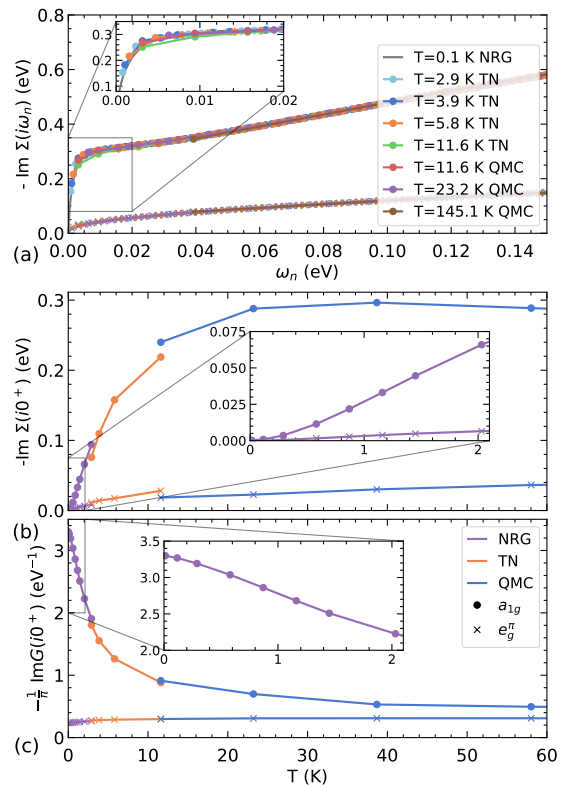


FIG. 2. (a) $\text{Im}\Sigma(i\omega_n)$ for the a_{1g} orbital (circles) and e_g^π orbitals (crosses) at various T from DFT+DMFT using QMC, TN, and NRG. Inset: zoom at low frequencies. (b) Scattering rate and (c) spectral function at the Fermi level as a function of T . Results at $i0^+$ in (b)–(c) for QMC and TN were obtained by fitting a fourth-order polynomial to the lowest eight Matsubara points. Insets in (b)–(c) magnify the FL behavior.

four-index tensor to the symmetrized Kanamori form (including spin-flip and pair-hopping terms) with three independent parameters. The optimal fit yields $U=3.94 \text{ eV}$, $U'=2.83 \text{ eV}$, and $J=0.56 \text{ eV}$, which violates the full rotational invariance ($U'=U-2J$) by only $\sim 0.01 \text{ eV}$.

We use DMFT to solve the effective many-body model, with a combination of impurity solvers to cover all T regimes (see [6] for details). First, we use the continuous-time hybridization-expansion QMC solver implemented in the TRIQS software library [30, 31] and its interface to electronic structure codes TRIQS/DFTTOOLS and TRIQS/SOLID_DMFT [6, 32, 33]. QMC calculations were performed down to 11.6 K (1/1000 eV). Second, the $T=0$ TN-based solver from [34–36] was extended to $T > 0$ using thermal-state purification [37, 38] and applied down to 2.9 K (1/4000 eV). Third, to access the sub-1 K regime, we use NRG, similarly as in Refs. [39, 40]. To make non-degenerate three-orbital NRG calculations tractable, we increase the local symmetry by neglecting the pair-hopping part of the interaction when using this solver [6, 39].

Crossover to a heavy FL—The emergence of the low- T heavy FL is illustrated in Fig. 2(a). It shows the imaginary part of the self-energy for each orbital as a function of Matsubara frequency for several T . The a_{1g} self-energy has a strong T dependence at low frequency, with a sudden decrease below the *onset temperature* $T_{\text{onset}} \sim 12$ K. This is a hallmark of strong correlations and corresponds to a sharp crossover from a high- T incoherent regime with a large scattering rate to a low- T coherent regime. This is further supported by Fig. 2(b), which shows the extrapolated zero-frequency value of the a_{1g} scattering rate $-\text{Im}\Sigma_{a_{1g}}(i0^+)$ as a function of T . The local spectral function (DOS) at the Fermi level $A_{a_{1g}}(0)$ correspondingly increases, as shown in Fig. 2(c). By contrast, the e_g^π self-energy is smaller and depends more weakly on temperature and frequency.

The FL fully develops only below the *FL coherence temperature* $T_{\text{FL}} \sim 1\text{--}2$ K, an order of magnitude smaller than T_{onset} . The FL regime is characterized by $-\text{Im}\Sigma \sim \omega^2 + \pi^2 T^2$ (see End Matter for $T = 0$ and Fig. 2(b) for $\omega = 0$) for the retarded self-energy and $\chi'' \sim \omega$ for the imaginary part of the retarded local spin susceptibility (see End Matter). The quasiparticle weights (from NRG at $T = 0$) are $Z_{a_{1g}} \approx 0.003$ and $Z_{e_g^\pi} \approx 0.03$.

Quasiparticle bandstructure—Figure 3(a) shows the momentum-resolved spectral function summed over orbitals at $T = 11.6$ K. The momentum-integrated spectral functions are displayed in panel (b) for several T . These results were obtained by analytic continuation of the QMC self-energies using Padé extrapolation, see Fig. 3(c)–(d), and are consistent with NRG [6].

We see from Fig. 3(b) that the onset of coherence is associated with the growth of a remarkably narrow quasiparticle peak at the Fermi level, in line with the small $Z_{a_{1g}}$. This corresponds to the formation of a flat band near the Fermi level (see panel (a)), together with the strong renormalization of the overall band structure (compare the black lines from DFT). The formation of the flat band can be understood from the fact that $\text{Re}\Sigma_{a_{1g}}(\omega)$ (panel (c)) exhibits a very steep rise near $\omega = 0$. As a result, the quasiparticle equation (quoting for simplicity a one-band version) $\omega - \text{Re}\Sigma(\omega) = \varepsilon_k - \mu$ has solutions ω_k which remain very close to zero energy for an extended range of momenta, as seen in panel (a) near the L-point.

Discussion—To elucidate the mechanism responsible for the strong correlations observed above, we first consider the effect of varying the Hund coupling J . Figure 4(a) shows the a_{1g} self-energy on the Matsubara axis at $T = 11.6$ K for various J . At small J , the self-energies are small; for $J \gtrsim 0.3$ eV, strong correlations develop. The self-energy becomes large and acquires the characteristic frequency dependence emphasized above (Fig. 2(a)). This frequency dependence is reminiscent of Hund metals in the ‘spin freezing’ regime [22, 23, 41] (see, e.g., Fig. 8 of Ref. [41]). Correspondingly, the extrapolated zero-

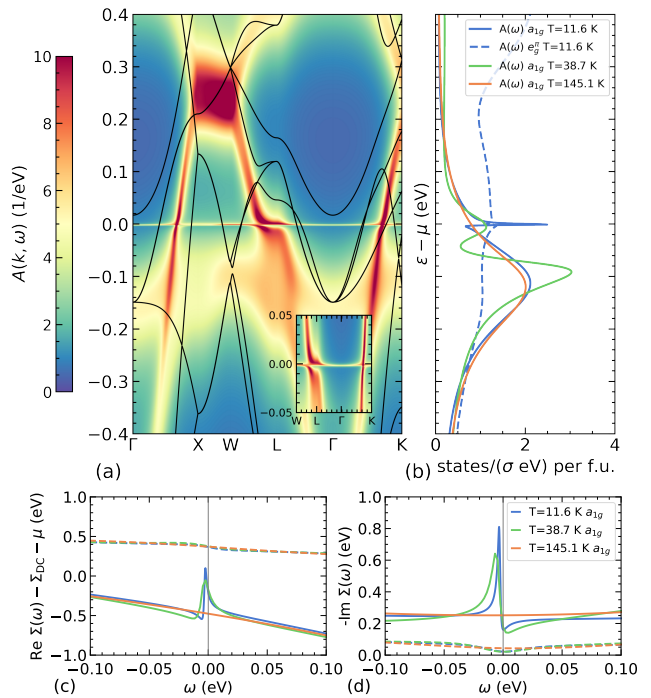


FIG. 3. (a) DFT+DMFT (QMC+Padé) k -resolved spectral function at $T = 11.6$ K (black lines give the DFT bands). Inset: zoom to the Fermi level, showing a flat quasiparticle band with suppressed spectral weight directly below $\omega = 0$. (b) DOS in the same energy range (see [6] for a wider range). The plain (dashed) blue line refers to the a_{1g} (e_g^π) orbital. The a_{1g} result at larger T is also shown. (c) Real and (d) imaginary part of the QMC+Padé real-frequency self-energies.

frequency scattering rate at finite T quickly increases as a function of J (inset of panel Fig. 4(a)), indicating a suppressed coherence scale. The Hund coupling is known to induce strong correlations through the ‘spin blocking’ mechanism, which forces electrons to keep a high-spin configuration while hopping between different sites. The dominance of high-spin configurations is indeed supported by the valence- and spin-resolved histograms, obtained with QMC, see Fig. 4(b), or NRG [6].

In Fig. 4(c), we show the a_{1g} and e_g^π orbital occupancies as a function of J . The Hund coupling induces a significant redistribution of orbital populations [18], with the occupancy of the a_{1g} orbital evolving from the DFT value ~ 0.4 to ~ 0.9 as J is increased beyond $J \sim 0.3$ eV. Hence, the a_{1g} orbital becomes $\sim 10\%$ hole-doped away from half-filling. This points at the relevance of Mott physics in this material, as proposed in Ref. [12].

To analyze the possible proximity of a Mott-insulating state, we perform a numerical experiment in which we add a crystal field to the Wannier Hamiltonian, while keeping the total d -electron count equal to 1.5 by adjusting the chemical potential. Figure 4(d) shows T_{FL} determined by NRG as a function of the a_{1g} orbital

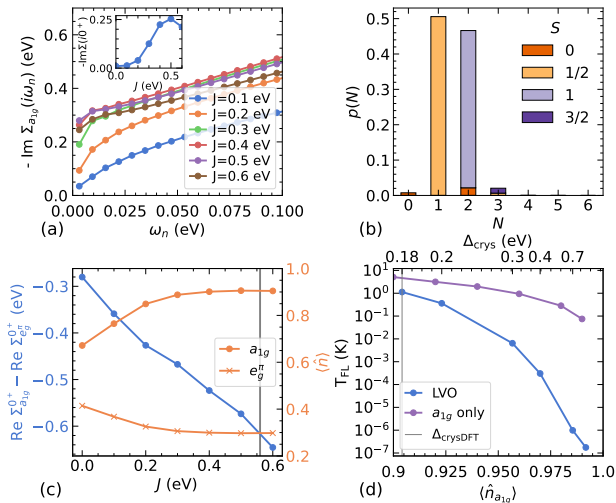


FIG. 4. (a) Evolution of $\Sigma_{a_{1g}}$ with increasing J at $T=11.6$ K. Results are obtained with the TN solver at fixed $U=3.94$ eV and $U'=U-2J$. Inset: scattering rate obtained as in Fig. 2(b). (b) Histogram displaying the statistical weights of the relevant multiplets in each valence (N) and spin (S) sector, obtained from QMC at $T=11.6$ K. (c) Evolution of the effective crystal field coming from $\text{Re}\Sigma(0)$ and of the orbital populations with increasing J . (d) T_{FL} for LVO as a function of the a_{1g} occupancy when changing the crystal field (as indicated in the top horizontal scale, see text) and for an effective model involving only the a_{1g} orbital, using the same intra-orbital U value. T_{FL} is estimated via the peak position of $\chi''(\omega)$ at $T=0$ from NRG (see End Matter). The vertical lines in panels (c) and (d) indicate the LVO values.

occupancy (lower horizontal scale) or the applied crystal field (upper scale). We see that T_{FL} is driven to remarkably low values as half-filling of the a_{1g} orbital is approached, with values as low as 10^{-6} K at 1% doping. This can be interpreted as the system reaching an orbital-selective Mott (OSM) phase [5, 14, 19–21] in which the e_g^π electrons remain itinerant while the a_{1g} ones basically localize, full localization being prevented at $T=0$ by inter-orbital hopping [26]. The relevance of the OSM phenomenon and of Hund physics as a possible cause for d -electron HF behavior was recently emphasized by Crispino et al. [5] and also previously mentioned qualitatively for LVO in the NMR study of Shimizu et al. [14].

While our results support the relevance of Mottness for LVO [12], they provide novel insights into the mechanism responsible for the HF behavior in LVO, namely the decisive role of Hund coupling and the wide range of permissible fillings. In Fig. 4(d), we compare T_{FL} of LVO, as a function of orbital occupancy, to that of a single-band model with the same DOS as the one of the a_{1g} orbital (also solved in DMFT). We see that, in order to reach a value of T_{FL} in the range 1–2 K, as observed in experiments, a tiny doping of $\sim 1\%$ is required in the single-band picture. By contrast, the small T_{FL} is robustly gen-

erated from the realistic multi-orbital description, as a result of orbital and Hund physics, in a wide range of a_{1g} doping. More broadly, our results emphasize that the multi-orbital character of the system is crucial, with inter-orbital correlations playing a key role, and hence that the e_g^π bands are not merely spectators.

Comparison to experiments—Finally, we discuss how our results compare to experimental observations. The resistivity, Hall effect, specific heat and susceptibility measurements on single crystals [3], as well as optical spectroscopy [42], all point to electronic coherence setting in below $T_{\text{onset}} \sim 10\text{--}30$ K. Above T_{onset} , LVO displays a large scattering rate and resistivity. This is consistent with our results in Fig. 2. Furthermore, a T^2 dependence of the resistivity is only observed below $T_{\text{FL}} \sim 2$ K, in excellent agreement with our estimate of $T_{\text{FL}} \sim 1\text{--}2$ K. The gradual emergence below T_{onset} of an extremely narrow quasiparticle peak reported in photoemission spectroscopy [43] also aligns with our Figs. 2(c) and 3(b). Angle-resolved photoemission experiments would be desirable to test the predictions of Fig. 3(a).

The low- T specific heat coefficient $C = \gamma T + \dots$ can be evaluated within DMFT from the zero-frequency spectral functions and quasiparticle weights of each orbital m as $\gamma = \frac{2\pi^2}{3} k_B^2 \sum_m A_m(0)/Z_m$. The bare DFT value from our calculated DOS is $\gamma_{\text{DFT}} = 17.1$ mJ/mol K $^{-2}$, in good agreement with previous theoretical estimates [7, 18]. Reported experimental values in the low- T HF regime are in the range $\gamma/\gamma_{\text{DFT}} \sim 25$ [1, 3] to ~ 30 [44]. A comparable value is reached in our DMFT calculations at $T \sim 8$ K, but, at low T , we overestimate $\gamma/\gamma_{\text{DFT}}$ by a large factor (~ 10). We note, however, that no clear saturation of C/T at low T is seen experimentally, and that further increase of γ at low T was reported on some samples [44, 45], so that the precise behavior of the specific heat of LVO at low T is yet to be fully clarified.

We conjecture that the overestimation of γ at low T comes from the intrinsic limitations of single-site DMFT. In this approach, γ is inversely proportional to Z , which we find to be tiny for the a_{1g} orbital. In a more accurate treatment beyond the single-site approximation, the inter-site magnetic exchange should intervene and reduce C/T by reducing the entropy associated with fluctuating local moments above T_{onset} . Indeed, slave-particle [46, 47] or cluster-DMFT calculations [48] yield, for a single band model, $\gamma/\gamma_{\text{DFT}} \sim 1/(Z + J_{\text{AF}}/\epsilon_{\text{F}})$ with J_{AF} the antiferromagnetic super-exchange and ϵ_{F} a typical (bare) electronic scale. In many oxides, the exchange term limits the value of γ as compared to the DMFT $1/Z$ enhancement. Remarkably, this effect appears to be much less pronounced in LVO, allowing γ to reach the large observed value. This is most likely due to frustration [14, 44, 45, 49–52] which results in a large amount of entropy stored at low T and hence a reduced value of the exchange term $J_{\text{AF}}/\epsilon_{\text{F}}$. NMR [53] and neutron scattering [51, 52] experiments yield estimates of the effec-

tive exchange between V-atoms in the range ~ 20 – 30 K, comparable to T_{onset} and significantly smaller than typical values in unfrustrated oxides. A proper description of the spin correlations probed by these experiments likely requires a treatment beyond single-site DMFT [6].

Outlook—The physical picture emerging from our work is that LVO is close to a Hund-assisted orbital selective Mott state. Recent experiments have indeed revealed that an insulating state can be induced by Li-intercalation [54] or, together with charge ordering, when subjecting this compound to uniaxial strain [55]. While some qualitative aspects of this physical picture were anticipated before [5, 12, 14], our work demonstrates how key progress on DMFT solvers now allows us to cover the full range of energy scales in this particularly challenging case and reliably establish the physical mechanism at hand. Our work also points at two necessary further developments: (i) including spatial fluctuations and computing spin and charge responses beyond single-site DMFT and (ii) exploring instabilities toward charge and spin ordering dependent on external perturbations such as pressure, uniaxial strain, and chemical substitutions.

Acknowledgements—We acknowledge useful discussions and communications with Ryotaro Arita, Sophie Beck, Riccardo Comin, Andrea Damascelli, Luca de’ Medici, Dongjin Oh, Dennis Huang, Xiangyu Luo, Giorgio Sangiovanni, Hidenori Takagi, Manish Verma, and Jan von Delft. M.G. and U.S. acknowledge support by the Deutsche Forschungsgemeinschaft (DFG, German Research Foundation) under Germany’s Excellence Strategy-426 EXC-2111-390814868. M.G. and U.S. are grateful to the Flatiron Institute and A.G. to the University of Munich for their hospitality. The Flatiron Institute is a division of the Simons Foundation.

* ahampel@flatironinstitute.org

- [1] S. Kondo, D. C. Johnston, C. A. Swenson, F. Borsa, A. V. Mahajan, L. L. Miller, T. Gu, A. I. Goldman, M. B. Maple, D. A. Gajewski, E. J. Freeman, N. R. Dilley, R. P. Dickey, J. Merrin, K. Kojima, G. M. Luke, Y. J. Uemura, O. Chmaissem, and J. D. Jorgensen, *LiV₂O₄: A heavy fermion transition metal oxide*, *Phys. Rev. Lett.* **78**, 3729 (1997).
- [2] H. Takagi, C. Urano, S. Kondo, M. Nohara, Y. Ueda, T. Shiraki, and T. Okubo, Transport properties of metallic LiV₂O₄ single crystals—heavy mass Fermi liquid behavior, *Materials Science and Engineering: B* **63**, 147–150 (1999).
- [3] C. Urano, M. Nohara, S. Kondo, F. Sakai, H. Takagi, T. Shiraki, and T. Okubo, LiV₂O₄ spinel as a heavy-mass Fermi liquid: Anomalous transport and role of geometrical frustration, *Phys. Rev. Lett.* **85**, 1052 (2000).
- [4] H.-A. Krug von Nidda, R. Bulla, N. Büttgen, M. Heinrich, and A. Loidl, Heavy fermions in transition metals and transition-metal oxides, *The European Physical Journal B - Condensed Matter and Complex Systems* **34**, 399 (2003).
- [5] M. Crispino, P. V. Arribi, A. Shukla, F. Hardy, A.-A. Haghighirad, T. Wolf, R. Heid, C. Meingast, T. Gorni, A. Avella, and L. de’ Medici, *Paradigm for finding *d*-electron heavy fermions: the case of Cr-doped CsFe₂As₂* (2023), [arXiv:2312.06511](https://arxiv.org/abs/2312.06511) [[cond-mat.str-el](https://arxiv.org/archive/cond)].
- [6] See supplemental material [*URL to be inserted by publisher*], which includes Refs. [1, 3, 14, 27–40, 45, 56–80], for details on the employed methods.
- [7] J. Matsuno, A. Fujimori, and L. F. Mattheiss, Electronic structure of spinel-type LiV₂O₄, *Phys. Rev. B* **60**, 1607 (1999).
- [8] D. J. Singh, P. Blaha, K. Schwarz, and I. I. Mazin, Electronic structure and heavy-fermion behavior in LiV₂O₄, *Phys. Rev. B* **60**, 16359 (1999).
- [9] V. I. Anisimov, M. A. Korotin, M. Zöfl, T. Pruschke, K. Le Hur, and T. M. Rice, Electronic structure of the heavy fermion metal LiV₂O₄, *Phys. Rev. Lett.* **83**, 364 (1999).
- [10] C. M. Varma, Heavy fermions in the transition-metal compound LiV₂O₄, *Phys. Rev. B* **60**, R6973 (1999).
- [11] J. Hopkinson and P. Coleman, LiV₂O₄: Frustration induced heavy fermion metal, *Phys. Rev. Lett.* **89**, 267201 (2002).
- [12] R. Arita, K. Held, A. V. Lukoyanov, and V. I. Anisimov, Doped Mott insulator as the origin of heavy-fermion behavior in LiV₂O₄, *Phys. Rev. Lett.* **98**, 166402 (2007).
- [13] K. Le Hur, Heavy electrons from Hund’s rule and short-range antiferromagnetism, *Phys. Rev. B* **75**, 014435 (2007).
- [14] Y. Shimizu, H. Takeda, M. Tanaka, M. Itoh, S. Niitaka, and H. Takagi, An orbital-selective spin liquid in a frustrated heavy fermion spinel LiV₂O₄, *Nature Communications* **3**, 981 (2012).
- [15] M. Onoda and S. Takada, T-linear resistivity and thermoelectric power in heavy-fermion spinel LiV₂O₄, *Journal of the Physical Society of Japan* **92**, 10.7566/jpsj.92.124706 (2023).
- [16] D. C. Johnston, C. A. Swenson, and S. Kondo, Specific heat (1.2–108 K) and thermal expansion (4.4–297 K) measurements of the 3*d* heavy-fermion compound LiV₂O₄, *Phys. Rev. B* **59**, 2627 (1999).
- [17] A. Georges, G. Kotliar, W. Krauth, and M. J. Rozenberg, Dynamical mean-field theory of strongly correlated fermion systems and the limit of infinite dimensions, *Rev. Mod. Phys.* **68**, 13 (1996).
- [18] I. A. Nekrasov, Z. V. Pchelkina, G. Keller, T. Pruschke, K. Held, A. Krimmel, D. Vollhardt, and V. I. Anisimov, Orbital state and magnetic properties of LiV₂O₄, *Phys. Rev. B* **67**, 085111 (2003).
- [19] V. Anisimov, I. Nekrasov, D. Kondakov, T. Rice, and M. Sgrist, Orbital-selective Mott-insulator transition in Ca_{2-x}Sr_xRuO₄, *The European Physical Journal B* **25**, 191–201 (2002).
- [20] S. Biermann, L. de’ Medici, and A. Georges, Non-Fermi-liquid behavior and double-exchange physics in orbital-selective Mott systems, *Phys. Rev. Lett.* **95**, 206401 (2005).
- [21] L. de’ Medici, S. R. Hassan, M. Capone, and X. Dai, Orbital-selective mott transition out of band degeneracy lifting, *Phys. Rev. Lett.* **102**, 126401 (2009).
- [22] P. Werner, E. Gull, M. Troyer, and A. J. Millis, Spin freezing transition and non-Fermi-liquid self-energy in a three-orbital model, *Phys. Rev. Lett.* **101**, 166405 (2008).

- [23] K. Haule and G. Kotliar, Coherence–incoherence crossover in the normal state of iron oxyphosphates and importance of Hund’s rule coupling, *New Journal of Physics* **11**, 025021 (2009).
- [24] A. Georges, L. d. Medici, and J. Mravlje, Strong correlations from Hund’s coupling, *Annual Review of Condensed Matter Physics* **4**, 137 (2013), <https://doi.org/10.1146/annurev-conmatphys-020911-125045>.
- [25] A. Georges and G. Kotliar, The Hund-metal path to strong electronic correlations, *Physics Today* **77**, 46–53 (2024).
- [26] F. B. Kugler and G. Kotliar, Is the orbital-selective Mott phase stable against interorbital hopping?, *Phys. Rev. Lett.* **129**, 096403 (2022).
- [27] A. A. Mostofi, J. R. Yates, G. Pizzi, Y.-S. Lee, I. Souza, D. Vanderbilt, and N. Marzari, An updated version of wannier90: A tool for obtaining maximally-localised Wannier functions, *Computer Physics Communications* **185**, 2309 (2014).
- [28] F. Aryasetiawan, M. Imada, A. Georges, G. Kotliar, S. Biermann, and A. I. Lichtenstein, Frequency-dependent local interactions and low-energy effective models from electronic structure calculations, *Phys. Rev. B* **70**, 1 (2004).
- [29] K. Nakamura, Y. Yoshimoto, Y. Nomura, T. Tadano, M. Kawamura, T. Kosugi, K. Yoshimi, T. Misawa, and Y. Motoyama, RESPACK: An ab initio tool for derivation of effective low-energy model of material, *Computer Physics Communications* **261**, 107781 (2021).
- [30] O. Parcollet, M. Ferrero, T. Ayril, H. Hafermann, I. Krivenko, L. Messio, and P. Seth, TRIQS: A toolbox for research on interacting quantum systems, *Computer Physics Communications* **196**, 398 (2015).
- [31] P. Seth, I. Krivenko, M. Ferrero, and O. Parcollet, TRIQS/CTHYB: A continuous-time quantum Monte Carlo hybridisation expansion solver for quantum impurity problems, *Computer Physics Communications* **200**, 274 (2016).
- [32] M. Aichhorn, L. Pourovskii, P. Seth, V. Vildosola, M. Zingl, O. E. Peil, X. Deng, J. Mravlje, G. J. Kraberger, C. Martins, M. Ferrero, and O. Parcollet, TRIQS/DFTTools: A TRIQS application for ab initio calculations of correlated materials, *Computer Physics Communications* **204**, 200 (2016).
- [33] M. E. Merkel, A. Carta, S. Beck, and A. Hampel, solid_dmft: gray-boxing DFT+DMFT materials simulations with TRIQS, *Journal of Open Source Software* **7**, 4623 (2022).
- [34] F. A. Wolf, A. Go, I. P. McCulloch, A. J. Millis, and U. Schollwöck, Imaginary-time matrix product state impurity solver for dynamical mean-field theory, *Phys. Rev. X* **5**, 041032 (2015).
- [35] N.-O. Linden, M. Zingl, C. Hubig, O. Parcollet, and U. Schollwöck, Imaginary-time matrix product state impurity solver in a real material calculation: Spin-orbit coupling in Sr_2RuO_4 , *Phys. Rev. B* **101**, 041101 (2020).
- [36] J. Karp, M. Bramberger, M. Grundner, U. Schollwöck, A. J. Millis, and M. Zingl, Sr_2MoO_4 and Sr_2RuO_4 : Disentangling the roles of Hund’s and van Hove physics, *Phys. Rev. Lett.* **125**, 166401 (2020).
- [37] F. Verstraete, J. J. García-Ripoll, and J. I. Cirac, Matrix product density operators: Simulation of finite-temperature and dissipative systems, *Phys. Rev. Lett.* **93**, 207204 (2004).
- [38] U. Schollwöck, The density-matrix renormalization group in the age of matrix product states, *Annals of Physics* **326**, 96 (2011), January 2011 Special Issue.
- [39] F. B. Kugler, M. Zingl, H. U. R. Strand, S.-S. B. Lee, J. von Delft, and A. Georges, Strongly correlated materials from a numerical renormalization group perspective: How the Fermi-liquid state of Sr_2RuO_4 emerges, *Phys. Rev. Lett.* **124**, 016401 (2020).
- [40] F. B. Kugler, C.-J. Kang, and G. Kotliar, Low-energy perspective on two-orbital Hund metals and the case of LaNiO_2 (2024), arXiv:2312.11457.
- [41] A. Kowalski, A. Hausoel, M. Wallerberger, P. Gu-nacker, and G. Sangiovanni, State and superstate sampling in hybridization-expansion continuous-time quantum Monte Carlo, *Phys. Rev. B* **99**, 155112 (2019).
- [42] P. E. Jönsson, K. Takenaka, S. Niitaka, T. Sasagawa, S. Sugai, and H. Takagi, Correlation-driven heavy-fermion formation in LiV_2O_4 , *Phys. Rev. Lett.* **99**, 167402 (2007).
- [43] A. Shimoyamada, S. Tsuda, K. Ishizaka, T. Kiss, T. Shimoyama, T. Togashi, S. Watanabe, C. Q. Zhang, C. T. Chen, Y. Matsushita, H. Ueda, Y. Ueda, and S. Shin, Heavy-fermion-like state in a transition metal oxide LiV_2O_4 single crystal: Indication of Kondo resonance in the photoemission spectrum, *Phys. Rev. Lett.* **96**, 026403 (2006).
- [44] H. Kaps, M. Brando, W. Trinkl, N. Büttgen, A. Loidl, E.-W. Scheidt, M. Klemm, and S. Horn, Heavy fermions in LiV_2O_4 : Kondo compensation versus geometric frustration, *Journal of Physics: Condensed Matter* **13**, 8497 (2001).
- [45] H. Okabe, M. Hiraishi, A. Koda, K. M. Kojima, S. Takeshita, I. Yamauchi, Y. Matsushita, Y. Kuramoto, and R. Kadono, Metallic spin-liquid-like behavior of LiV_2O_4 , *Phys. Rev. B* **99**, 041113 (2019).
- [46] G. Kotliar, The large N expansion and the strong correlation problem, in *Strongly Interacting Fermions and High- T_c superconductivity*, Les Houches, Session LVI, edited by B. Doucot and J. Zinn-Justin (Elsevier, 1995) p. 197.
- [47] S. Florens and A. Georges, Slave-rotor mean-field theories of strongly correlated systems and the Mott transition in finite dimensions, *Phys. Rev. B* **70**, 035114 (2004).
- [48] O. Parcollet, G. Biroli, and G. Kotliar, Cluster dynamical mean field analysis of the Mott transition, *Phys. Rev. Lett.* **92**, 226402 (2004).
- [49] S. Burdin, D. R. Grempel, and A. Georges, Heavy-fermion and spin-liquid behavior in a Kondo lattice with magnetic frustration, *Phys. Rev. B* **66**, 045111 (2002).
- [50] M. S. Laad, L. Craco, and E. Müller-Hartmann, Heavy-fermion behavior of the spinel-based transition-metal oxide LiV_2O_4 , *Phys. Rev. B* **67**, 033105 (2003).
- [51] S.-H. Lee, Y. Qiu, C. Broholm, Y. Ueda, and J. J. Rush, Spin fluctuations in a magnetically frustrated metal LiV_2O_4 , *Phys. Rev. Lett.* **86**, 5554 (2001).
- [52] K. Tomiyasu, K. Iwasa, H. Ueda, S. Niitaka, H. Takagi, S. Ohira-Kawamura, T. Kikuchi, Y. Inamura, K. Nakajima, and K. Yamada, Spin-orbit fluctuations in frustrated heavy-fermion metal LiV_2O_4 , *Phys. Rev. Lett.* **113**, 236402 (2014).
- [53] A. V. Mahajan, R. Sala, E. Lee, F. Borsa, S. Kondo, and D. C. Johnston, ^7Li and ^{51}V NMR study of the heavy-fermion compound LiV_2O_4 , *Phys. Rev. B* **57**, 8890 (1998).

- [54] T. Yajima, T. Soma, K. Yoshimatsu, N. Kurita, M. Watanabe, and A. Ohtomo, Heavy-fermion metallic state and Mott transition induced by li-ion intercalation in LiV_2O_4 epitaxial films, *Phys. Rev. B* **104**, 245104 (2021).
- [55] U. Niemann, Y.-M. Wu, R. Oka, D. Hirai, Y. Wang, Y. E. Suyoğlu, M. Kim, P. A. van Aken, and H. Takagi, Crystallization of heavy fermions via epitaxial strain in spinel LiV_2O_4 thin film, Proceedings of the National Academy of Sciences **120**, 10.1073/pnas.2215722120 (2023).
- [56] D. R. Hamann, Optimized norm-conserving Vanderbilt pseudopotentials, *Phys. Rev. B* **88**, 085117 (2013).
- [57] M. van Setten, M. Giantomassi, E. Bousquet, M. Verstraete, D. Hamann, X. Gonze, and G.-M. Rignanese, The PseudoDojo: Training and grading a 85 element optimized norm-conserving pseudopotential table, *Computer Physics Communications* **226**, 39 (2018).
- [58] E. Şaşıoğlu, C. Friedrich, and S. Blügel, Effective Coulomb interaction in transition metals from constrained random-phase approximation, *Phys. Rev. B* **83**, 121101 (2011).
- [59] H. LaBollita, J. Kaye, and A. Hampel, Stabilizing the calculation of the self-energy in dynamical mean-field theory using constrained residual minimization (2023), [arXiv:2310.01266 \[cond-mat.str-el\]](https://arxiv.org/abs/2310.01266).
- [60] C. Hubig, F. Lachenmaier, N.-O. Linden, T. Reinhard, L. Stenzel, A. Swoboda, M. Grundner, and S. Mardazad, The SYTEN toolkit.
- [61] M. Caffarel and W. Krauth, Exact diagonalization approach to correlated fermions in infinite dimensions: Mott transition and superconductivity, *Phys. Rev. Lett.* **72**, 1545 (1994).
- [62] S. Paeckel, T. Köhler, A. Swoboda, S. R. Manmana, U. Schollwöck, and C. Hubig, Time-evolution methods for matrix-product states, *Annals of Physics* **411**, 167998 (2019).
- [63] M. Yang and S. R. White, Time-dependent variational principle with ancillary Krylov subspace, *Physical Review B* **102**, 10.1103/physrevb.102.094315 (2020).
- [64] J. Haegeman, J. I. Cirac, T. J. Osborne, I. Pižorn, H. Verschelde, and F. Verstraete, Time-dependent variational principle for quantum lattices, *Phys. Rev. Lett.* **107**, 070601 (2011).
- [65] J. Haegeman, C. Lubich, I. Oseledets, B. Vandereycken, and F. Verstraete, Unifying time evolution and optimization with matrix product states, *Phys. Rev. B* **94**, 165116 (2016).
- [66] M. Yang and S. R. White, *Time dependent variational principle with ancillary Krylov subspace* (2020).
- [67] M. Grundner, T. Blatz, J. Sous, U. Schollwöck, and S. Paeckel, Cooper-paired bipolaronic superconductors (2023), [arXiv:2308.13427 \[cond-mat.supr-con\]](https://arxiv.org/abs/2308.13427).
- [68] C. Bertrand, D. Bauernfeind, P. T. Dumitrescu, M. Maček, X. Waintal, and O. Parcollet, Quantum quasi Monte Carlo algorithm for out-of-equilibrium green functions at long times, *Phys. Rev. B* **103**, 155104 (2021).
- [69] R. Bulla, A. C. Hewson, and T. Pruschke, Numerical renormalization group calculations for the self-energy of the impurity Anderson model, *Journal of Physics: Condensed Matter* **10**, 8365 (1998).
- [70] R. Peters, T. Pruschke, and F. B. Anders, Numerical renormalization group approach to Green's functions for quantum impurity models, *Phys. Rev. B* **74**, 245114 (2006).
- [71] A. Weichselbaum and J. von Delft, Sum-rule conserving spectral functions from the numerical renormalization group, *Phys. Rev. Lett.* **99**, 076402 (2007).
- [72] S.-S. B. Lee, F. B. Kugler, and J. von Delft, Computing local multipoint correlators using the numerical renormalization group, *Phys. Rev. X* **11**, 041007 (2021).
- [73] A. Weichselbaum, Non-abelian symmetries in tensor networks: A quantum symmetry space approach, *Ann. Phys.* **327**, 2972 (2012); Tensor networks and the numerical renormalization group, *Phys. Rev. B* **86**, 245124 (2012); X-symbols for non-abelian symmetries in tensor networks, *Phys. Rev. Research* **2**, 023385 (2020).
- [74] R. Žitko and T. Pruschke, Energy resolution and discretization artifacts in the numerical renormalization group, *Phys. Rev. B* **79**, 085106 (2009).
- [75] S.-S. B. Lee and A. Weichselbaum, Adaptive broadening to improve spectral resolution in the numerical renormalization group, *Phys. Rev. B* **94**, 235127 (2016).
- [76] S.-S. B. Lee, J. von Delft, and A. Weichselbaum, Doublon-holon origin of the subpeaks at the Hubbard band edges, *Phys. Rev. Lett.* **119**, 236402 (2017).
- [77] F. B. Kugler, Improved estimator for numerical renormalization group calculations of the self-energy, *Phys. Rev. B* **105**, 245132 (2022).
- [78] A. K. Mitchell, M. R. Galpin, S. Wilson-Fletcher, D. E. Logan, and R. Bulla, Generalized Wilson chain for solving multichannel quantum impurity problems, *Phys. Rev. B* **89**, 121105 (2014).
- [79] K. M. Stadler, A. K. Mitchell, J. von Delft, and A. Weichselbaum, Interleaved numerical renormalization group as an efficient multiband impurity solver, *Phys. Rev. B* **93**, 235101 (2016).
- [80] S. Kondo, C. Urano, Y. Kurihara, M. Nohara, and H. Takagi, From the geometrically frustrated antiferromagnets ZnV_2O_4 and ZnCr_2O_4 to the heavy-mass Fermi liquid LiV_2O_4 , in *Magnetic Excitations in Strongly Correlated Electrons*, Proceedings of the International Workshop on Magnetic Excitations in Strongly Correlated Electrons August 19-22, 1999 Hamamatsu, Japan, edited by M. Takigawa, K. Ueda, and Y. Ueda (J. Phys. Soc. Jpn. 69 Suppl. B., 2000) p. 139.

END MATTER

Appendix: Real-frequency dynamics—We include, for completeness, several numerical results obtained directly in real frequencies from DFT+DMFT calculations using the NRG impurity solver. Figure 5 shows the local spectral function and the real part of the self-energy of the a_{1g} orbital on linear scales. The main panels give an overview at a large frequency range from -4 eV to 3 eV. The results from three choices of temperatures below 3 K completely overlap. Close to zero frequency, one notices a strikingly sharp low-energy feature. The insets, magnifying this low-energy feature, reveal how the quasiparticle peak (top panel) builds up with decreasing temperature and the slope of $\text{Re}\Sigma$ (bottom panel) increases, corresponding to a decreasing quasiparticle weight.

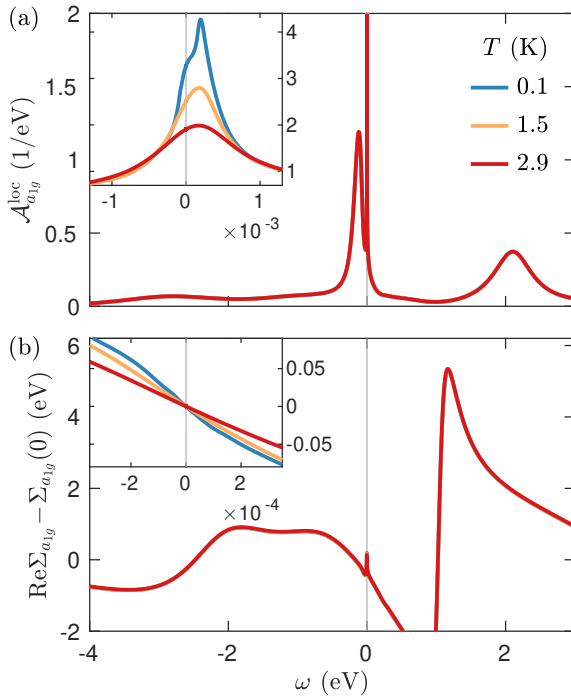


FIG. 5. (a) Local spectral function and (b) real part of the self-energy of the a_{1g} orbital, for three choices of low temperature values, on linear scales.

Figure 6 shows the imaginary parts of the a_{1g} self-energy and of the local spin susceptibility on logarithmic scales, obtained at $T = 0$. Colors indicate three choices of the crystal field; $\Delta \approx 0.18$ is the appropriate value for LVO, and larger Δ is used to approach an OSM state. The top panel demonstrates the large scattering rate in the incoherent regime at finite energies and the crossover to FL behavior $-\text{Im}\Sigma \sim \omega^2$ at extremely low frequencies. The bottom panel supports this picture: The incoherent regime is characterized by an extremely large spin susceptibility, while, in the FL regime, $\chi'' \sim \omega$ decreases as energy is decreased. The peak position of χ'' , ω_{max} , can be used to estimate T_{FL} (e.g., $T_{\text{FL}} = \omega_{\text{max}}/2$). The result for LVO ($\Delta \approx 0.18$) is roughly 0.1 meV or 1 K.

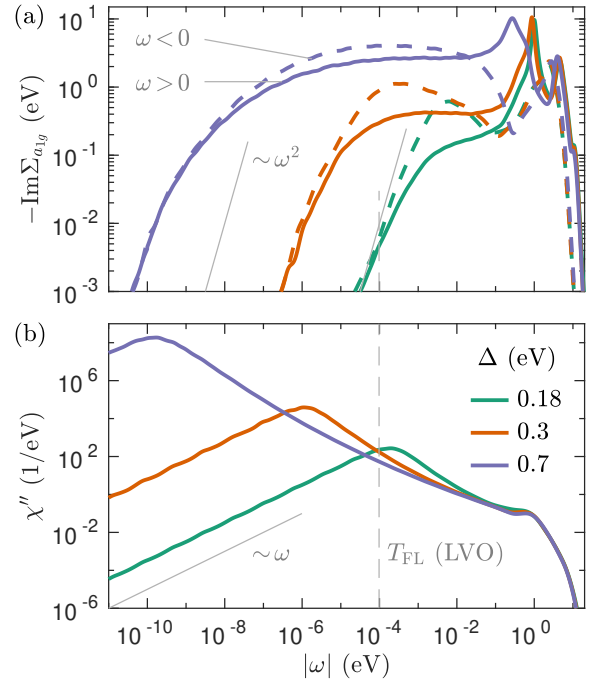








FIG. 6. Imaginary parts of (a) the self-energy of the a_{1g} orbital and (b) the local spin susceptibility, for three choices of crystal-field splitting, on logarithmic scales.

Supplemental Material

LiV₂O₄: Hund-Assisted Orbital-Selective Mottness

M. Grundner ^{1,2} F. B. Kugler ³ O. Parcollet ^{3,4} U. Schollwöck ^{1,2} A. Georges ^{5,3,6,7} and A. Hampel ^{3,*}

¹*Department of Physics and Arnold Sommerfeld Center for Theoretical Physics (ASC), Ludwig-Maximilians-Universität München, D-80333 Munich, Germany*

²*Munich Center for Quantum Science and Technology (MCQST), D-80799 München, Germany*

³*Center for Computational Quantum Physics, Flatiron Institute, 162 5th Avenue, New York, NY 10010, USA*

⁴*Université Paris-Saclay, CNRS, CEA, Institut de Physique Théorique, 91191, Gif-sur-Yvette, France*

⁵*Collège de France, 11 Place Marcelin Berthelot, 75005 Paris, France*

⁶*CPHT, CNRS, Ecole Polytechnique, IP Paris, F-91128 Palaiseau, France*

⁷*DQMP, University of Geneva, 24 quai Ernest-Ansermet, 1211 Geneva, Switzerland*

(Dated: September 27, 2024)

In this Supplemental Material, we give computational details of all employed methods, DFT and cRPA, QMC, TN, and NRG, and finally discuss magnetic order in LVO.

S1. DFT AND LOW-ENERGY MODEL

Density-functional theory (DFT) calculations are performed using the QUANTUM ESPRESSO (QE) software package fixing the structure parameters to the experimental values reported for 12 K $a_0=8.226\,94(3)$ Å and $x_{\text{O}} = 0.26109(2)$ [S1]. We performed calculations using the ONCVSP norm-conserving pseudopotentials [S2, S3] in conjunction with the Perdew–Burke–Ernzerhof (PBE) exchange–correlation functional. We use a wavefunction cut-off of 90 Ry, and a density cut-off of 360 Ry, resulting in an energy error of <1 meV per formula unit. A mesh of $11 \times 11 \times 11$ k -points has been chosen, matching this total energy error requirement.

Further, we construct maximally localized Wannier functions (MLWFs) using WANNIER90 (W90) [S4] for the low-energy states around the Fermi level with dominantly V d -character. This allows us to define a low-energy Hamiltonian $H^{\text{W90}}(\mathcal{R})$ in real space, capturing the essential physics of the system realistically. Furthermore, we rotate the Hamiltonian on each V -site into the crystal-field basis to diagonalize both the local non-interacting Hamiltonian and the hybridization function. For high accuracy low-temperature calculations, we leverage Wannier interpolation, Fourier transforming $H^{\text{W90}}(\mathcal{R})$ to a dense $41 \times 41 \times 41$ k -point mesh to avoid any k -discretization error. We followed this procedure for both an effective 12 band model (a_{1g} plus e_g^π orbitals) and an effective 20 band model (all five d -orbitals per V site).

We used the constrained random phase approximation (cRPA) [S5] as implemented in the RESPACK code [S6] to determine the effective Coulomb interaction for our low-energy model. By separating the electronic structure into a subspace near the Fermi level and the rest of

the system we calculate the effective partially screened Coulomb interaction that can be identified as the effective interaction in our low-energy model. Formally, this means the separation of the total electronic polarizability $P = P_{\text{sub}} + P_{\text{rest}}$ where P_{sub} is the polarizability for the correlated subspace and P_{rest} is for the rest of the system. Then, the screened Coulomb tensor can be calculated in a local basis from the bare Coulomb interaction tensor \mathbf{V} , as $\mathbf{U}(\omega) = \mathbf{V}/[1 - \mathbf{V}P_{\text{rest}}(\omega)]$. We used the same well-localized correlated subspace basis for cRPA as used within DMFT, i.e., contributions to the polarizability for the target space are removed via their overlap with the Kohn–Sham states [S7], and the screened and bare Coulomb integrals are then evaluated in the maximally localized Wannier orbitals basis set of the correlated subspace treated in DMFT. Here, we limit ourselves to the static limit $\mathbf{U}(\omega = 0)$ of the screened interaction. We further post-process $\mathbf{U}(\omega = 0)$ to obtain a symmetrized Kanamori form of the interaction, which is easier to treat by the impurity solvers.

The Kanamori interaction Hamiltonian has the form

$$\begin{aligned} \hat{H}_U &= \frac{1}{2} \sum_{\sigma} \sum_i U \hat{n}_{i\sigma} \hat{n}_{i\bar{\sigma}} \\ &+ \frac{1}{2} \sum_{\sigma} \sum_{i \neq j} [U' \hat{n}_{i\sigma} \hat{n}_{j\bar{\sigma}} + (U' - J) \hat{n}_{i\sigma} \hat{n}_{j\sigma}] \\ &+ \frac{1}{2} \sum_{\sigma} \sum_{i \neq j} [J c_{i\sigma}^\dagger c_{j\bar{\sigma}}^\dagger c_{i\bar{\sigma}} c_{j\sigma} + J c_{i\sigma}^\dagger c_{i\bar{\sigma}}^\dagger c_{j\bar{\sigma}} c_{j\sigma}]. \end{aligned} \quad (\text{S1})$$

Here, i, j mark different orbitals, but the same side, σ marks spin, and $\hat{n} = c^\dagger c$ is the density operator. We solve the interacting many-body model in a one-shot fashion, i.e., without charge density updates to the DFT code. DMFT calculations (except those with NRG as impurity solver) are performed utilizing the TRIQS software library [S8], and its interface to electronic structure codes TRIQS/DFTTOOLS [S9].

* ahampel@flatironinstitute.org

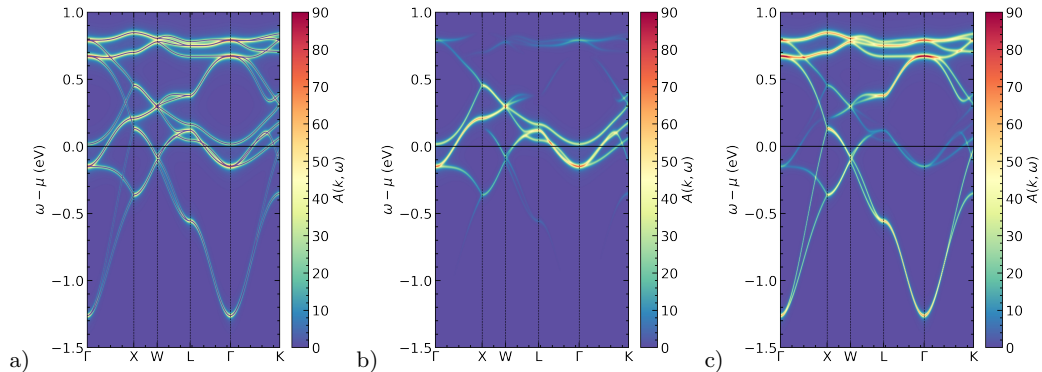


FIG. S1. DFT band structure and DOS calculated by wannier90 for the 12 orbital low-energy model for the a_{1g} and e_g^π bands around the Fermi level. (a) band structure calculated from the wannier90 model Hamiltonian (gray lines), and the corresponding non interacting spectral function with small broadening applied. (b) Spectral function projection on the a_{1g} orbital on each of the four V-sites. (c) Projection on the two e_g^π orbitals on each V-site.

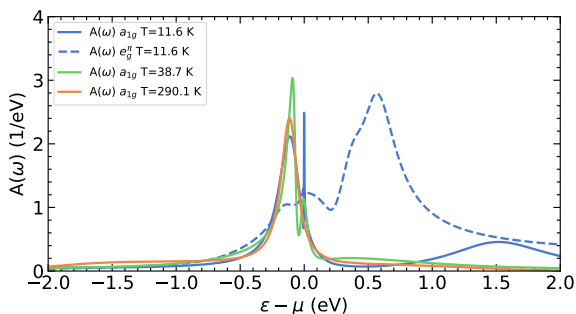


FIG. S2. DOS from DMFT (QMC) by analytically continuing the Matsubara self-energy and integrating the real-frequency lattice Green's function. The solid (dashed) blue line refers to the a_{1g} (e_g^π) orbital at $T=11.6$ K. The a_{1g} result at larger T is also shown. Results are identical to Fig. 3(b) of the main text, but shown at larger energy range.

S2. QUANTUM MONTE CARLO

We employ quantum Monte Carlo (QMC)-based solvers in the hybridization-expansion formulation using TRIQS/CTHYB [S10] and TRIQS/SOLID_DMFT [S11]. The solvers take into account all off-diagonal and also non density-density terms. Typically, the DMFT cycle is converged so that $|G_{\text{imp}} - G_{\text{loc}}| < 10^{-4}$, but we additionally monitored explicitly the convergence of the impurity self-energy at the first few Matsubara frequencies to reliably investigate the low-energy physics. At low energies we required that the change in self-energy values between DMFT iterations is ~ 1 meV. QMC calculations were performed from 290 K down to 11.6 K. To achieve the aforementioned accuracy, 5×10^7 independent measurements of G_{imp} are performed in the final dynamical mean-field theory (DMFT) iteration, the number of Matsubara frequencies is increased to up to 4×10^4 during the DMFT step at low temperatures, and the number of

τ points is increased to 4×10^5 when measuring the fast decaying impurity Green function in TRIQS/CTHYB. At very low temperatures, the warm-up time to thermalize QMC is substantial in this system, with the chosen interaction parameters, and up-to 10^5 warm-up cycles on each MC walker are necessary to thermalize and remove any spurious behavior in Σ_{imp} , which takes around 24 hours per impurity solver call. High-frequency noise in the impurity self-energy is suppressed by fitting the tail of Σ_{imp} up to fourth order in a window with moderate noise. The first two moments of the tail expansion, i.e., the Hartree shift $\text{Re}\Sigma_{\text{imp}}(i\omega_n \rightarrow \infty)$ and the leading order decay of $\text{Im}\Sigma_{\text{imp}}(i\omega_n)$, are measured to high precision directly in TRIQS/CTHYB [S12] and fixed in the fitting, stabilizing the DMFT convergence.

In Fig. S2, we show the local spectral function (DOS) obtained from QMC in a larger energy window range compared to Fig. 3(b) in the main text. An upper Hubbard band of the a_{1g} orbital can be observed at around 1.5 eV.

S3. TENSOR NETWORKS

We use a tensor network solver for the DMFT impurity problem operating on the Matsubara axis [S13, S14]. Green's functions are obtained via time evolution in imaginary time and subsequent Fourier transformation [S13]. Calculations are performed using matrix product states (MPS) as implemented in the SYTEN tensor network library [S15].

The impurity interaction terms are given by the Hubbard-Kanamori Hamiltonian as defined in equation (S1) with interaction parameters as determined above. Onsite energies and impurity-bath hoppings are obtained from fitting the hybridization function [S13, S16, S17]. Calculations were performed using matrix product states (MPS) with the three impurity orbitals I_1 , I_2 , and I_3 grouped together with their associated bath

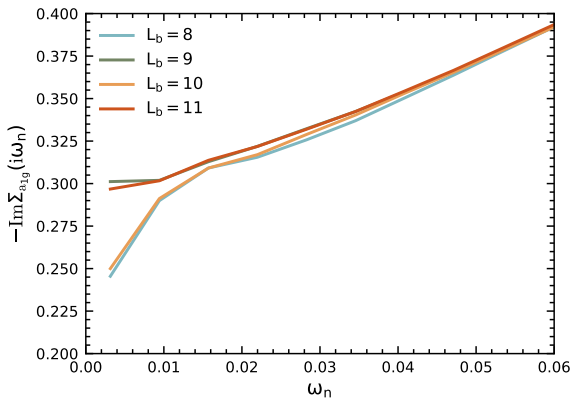


FIG. S3. Odd-even effect in bath size of TN-based simulations at $\beta = 1000$. The even bath sizes give the physical result.

orbitals B_1 , B_2 , and B_3 kept in vicinity. Results in the main text are shown for $L_b = 10$ bath sites per impurity orbital. We exploited all 5 symmetries of the Hamiltonian, namely particle number conservation ($U(1)$), spin degeneracy ($SU(2)$), and band parity conservation (Z_2) for each band.

We extended our zero-temperature impurity solver [S13, S14, S17] using the purification technique [S18, S19]. Calculations were performed in a temperature range from a few hundred K down to 2.9 K ($\beta = 4000$ eV $^{-1}$). In these calculations, the physical thermal state $\rho_P(\beta)$ is represented by tracing over the auxiliary degrees of freedom of a pure state $|\psi_\beta\rangle$ living in a Hilbert space of physical (P) and auxiliary (A) degrees of freedom

$$\rho_P(\beta) = \text{Tr}_A |\psi_\beta\rangle \langle \psi_\beta| \quad (\text{S2})$$

where we get $|\psi_\beta\rangle$ by an imaginary time-evolution

$$|\psi_\beta\rangle = (e^{-\beta \hat{H}_P/2} \otimes \hat{I}_A) |\psi_0\rangle. \quad (\text{S3})$$

Here, \hat{H}_P is the actual physical Hamiltonian, and \hat{I}_A the identity acting on the auxiliary degrees of freedom. The requirement on $|\psi_0\rangle$ is that $\text{Tr}_A |\psi_0\rangle \langle \psi_0| = \hat{I}_P$, the (unnormalized) infinite-temperature thermal state. All thermal expectation values can then be expressed as pure state expectation values $\langle \psi_\beta | \dots | \psi_\beta \rangle / Z_\beta$ with $Z_\beta = \langle \psi_\beta | \psi_\beta \rangle$. Here, we choose as $|\psi_0\rangle$ the product state of maximally entangled states on pairs of physical and ancilla orbitals given by

$$|\psi_0^i\rangle = \frac{1}{2} (|0, \uparrow \downarrow\rangle + |\uparrow, \downarrow\rangle + |\downarrow, \uparrow\rangle + |\uparrow \downarrow, 0\rangle), \quad (\text{S4})$$

expressed in $SU(2)$ invariant form. Due to the high accuracy required in the imaginary time evolution, we used a combination of several time evolution techniques, while keeping a maximum of 1536 $SU(2)$ states (corresponding to about 5000 $U(1)$ states) and using a truncated weight of $w_t = 10^{-11}$ throughout. We used the global

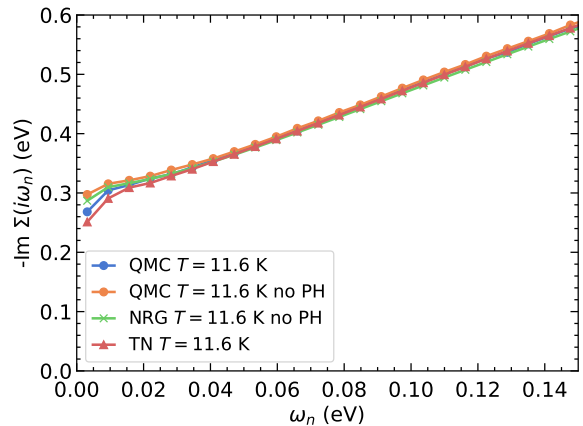


FIG. S4. Effect of pair hopping on the Matsubara self-energy.

Krylov method [S20] up to imaginary time $\tau = 0.5$ eV $^{-1}$, the global subspace expansion method (GSE) [S21] up to $\tau = 5$ eV $^{-1}$ followed by two-site TDVP [S22, S23] up to $\tau = 20$ eV $^{-1}$ and the local subspace expansion method (LSE) [S24, S25] up to $\tau = \beta/2$. We found it helpful to use exponentially increasing time steps $\delta\tau_n = \min(0.1 \times 1.01^n, 0.5)$ eV $^{-1}$ during thermal state preparation to limit the impact of truncation and projection errors.

During the imaginary time evolution of our excited states for the calculation of the impurity Green's functions we again used a truncated weight of $w_t = 10^{-11}$ and allowed for a maximum of 1536 $SU(2)$ states. Here, we used GSE up to $\tau = 2$ eV $^{-1}$ followed by two-site TDVP [S22, S23] up to $\tau = 25$ eV $^{-1}$ and LSE for the remainder of the time evolution up to $\tau = \beta/2$. Using either the GSE method or the global Krylov method for at least a single time step in the beginning is essential to ensure correct results, due to the inability of two-site TDVP to produce the necessary basis states immediately after a local excitation [S20, S21, S26].

As an example of the resulting accuracy, we consider the occupancy of the degenerate bands at the very low temperature $\beta = 4000$ eV $^{-1}$, which is given by 0.29872814 and 0.29875236 respectively, with a deviation of 2.4×10^{-5} . To improve the numerical accuracy of the calculation of self-energies we used an improved estimator presented in [S27].

At the lowest temperatures, the TN calculations produce a low-energy spectrum which depends on the parity of the bath sizes (and the resulting particle numbers) beyond expectable finite-size effects. This odd-even effect in particle numbers originates from the a_{1g} orbital where there is one bath site with an on-site energy very close to zero (at $\beta = 1000$, -0.0035 eV for $L_b = 9$ and -0.00087 eV for $L_b = 10$) which has an occupation by one particle more or less. At the same time, the differences in the chemical potentials between $L_b = 9$ and $L_b = 10$ are about 0.0039 eV. The differences in the hybridization

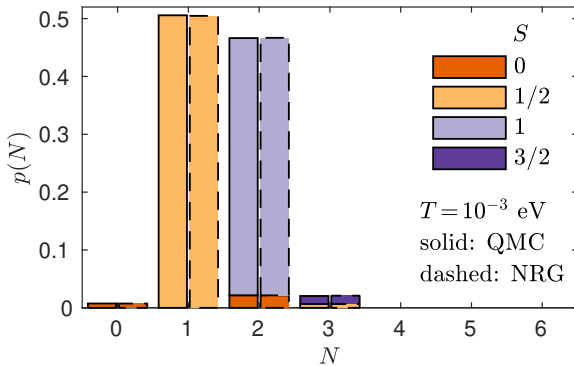


FIG. S5. Valence histogram obtained from QMC and NRG.

functions $\Delta_{a_{1g}}$ for $L_b = 9$ and $L_b = 10$ are notable only for the first two Matsubara frequencies for this β and of order $\mathcal{O}(10^{-3})$ and $\mathcal{O}(10^{-4})$ respectively. The crux is that these respective energy scales to be resolved are at the limit of the currently possible.

The physical choice that the correct results are obtained for the *even* bath sizes (with total spin $S = 0$ in $T = 0$ calculations which we also carried out) rests theoretically on the handshake with the QMC results at $\beta = 1000$ and with NRG results at $\beta = 4000$. Additionally, it is supported by the experimental knowledge that LiV_2O_4 (LVO) is a Fermi liquid at very low T , indicating that total spin $S = 0$ prevails at very low T .

S4. NUMERICAL RENORMALIZATION GROUP

We use the full density-matrix NRG [S28, S29] in an implementation [S30] based on the QSpace tensor library [S31]. We employ z -averaging [S32], adaptive broadening [S33, S34], a symmetric improved self-energy estimator [S35] and interleave the Wilson chains [S36, S37]. The number of z shifts is $n_z = 3$; the NRG discretization parameter is $\Lambda = 6$; we interleave the three Wilson chains (one chain per orbital) and keep up to $N_{\text{keep}} = 4 \times 10^5$ $SU(2)$ multiplets during the iterative diagonalization.

Similarly as in Refs. [S38, S39], we neglect the pair-hopping part of the Kanamori Hamiltonian, i.e., the very last term in Eq. (S1). Thereby, the charge per orbital is conserved, and the local symmetry is increased from $U(1) \otimes SU(2) \otimes (Z_2)^3$ to $SU(2) \otimes (U(1))^3$. This simplification makes the NRG calculations considerably more efficient and was found to have only mild impact on the low-energy physics in Ref. [S38]. In Fig. S4, we compare results with (QMC and TN) and without (QMC and NRG) pair hopping in the present context and again find that the effect is only mild. Furthermore, Fig. S5 shows the valence histogram, i.e., the probability of different impurity configurations. The results between QMC and NRG at $T = 1/1000$ eV agree perfectly. NRG results at lower T differ from those at $T = 1/1000$ eV only marginally.

S5. MAGNETIC CORRELATIONS AND ORDERING IN DMFT

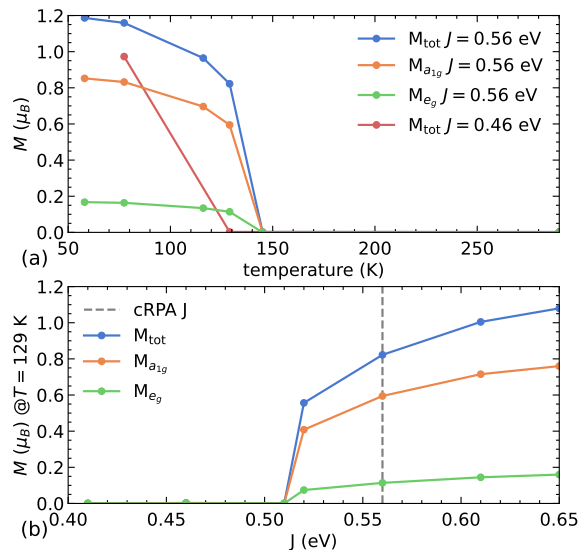


FIG. S6. (a) Orbital-resolved magnetic moments from DMFT (calculated via QMC) at fixed $U = 3.94$ eV and $U' = 2.83$ eV. For $J = 0.56$ eV, the system orders FM in single-site DMFT with a strong local moment in the a_{1g} orbitals. (b) Magnetic moment calculated via QMC at $T = 129$ K and varying J .

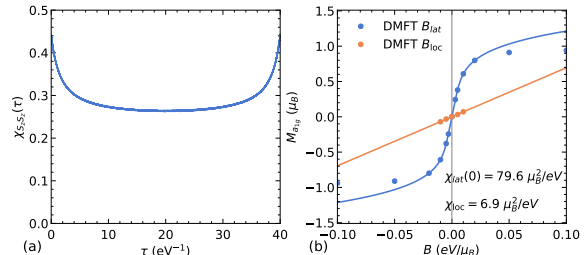


FIG. S7. (a) Impurity susceptibility $\chi_{S_z S_z}(\tau)$ measured at $T = 290.1$ K via QMC at the cRPA interaction values. (b) Magnetic moment as function of an applied magnetic field locally and on the lattice calculated via QMC at $T = 290.1$ K using cRPA interaction values. Lines show a first-order (B_{loc}) and fifth-order (B_{lat}) polynomial fit.

In the calculations shown in the main text, we focused only on the non-magnetic solution of the DMFT equations; technically this is done by enforcing a paramagnetic state in each DMFT iteration. We also performed calculations allowing for ferromagnetic ordering and observed a clear tendency of the system to order ferromagnetically (FM) just below 150 K, as shown in Fig. S6(a). From Fig. S6(b), it can be observed that the ordering temperature depends strongly on the Hund coupling J . We also tried to stabilize simple antiferromagnetic order

by solving four independent impurity problems in the unit cell without any sign of ordering.

In Fig. S7, we display for $T = 290$ K the imaginary-time dependence of the local susceptibility (panel (a)) as well as (panel (b)) the local (χ_{imp}) and $\mathbf{q} = 0$ uniform (χ_{lat}) static susceptibilities. The latter are obtained by applying an external Zeeman field, either locally or uniformly, and computing the resulting magnetization.

We observe that the local susceptibility tends to a constant at large time, indicating the presence of local moments at the temperature considered (which is way above the onset of coherence). Furthermore, the uniform susceptibility is larger than the local one, indeed consistent with a tendency to ferromagnetic inter-site correlations.

These observations raise questions that should be addressed in future work and most likely require to go beyond a single-site DMFT computation. The presence

of local moments above the onset temperature for coherence is indeed consistent with experimental observations, such as the Curie–Weiss form of the magnetic susceptibility [S40] and observations from NMR [S41] and μ SR [S42]. The fact that Zn substitutions on the lithium sites induce spin-glass ordering is also revealing in this respect [S43]. In contrast, the tendency to ferromagnetic correlations is at odds with neutrons and NMR experiments which reveal a dominantly antiferromagnetic exchange, and no long-range order has been reported down to the lowest temperature investigated (which motivates our calculations focused on the paramagnetic phase). We conjecture that strong spatial fluctuations in this frustrated system must be taken into account to properly describe its magnetic properties, hence providing motivation for future work using either cluster or vertex-based extensions of DMFT.

-
- [S1] S. Kondo, D. C. Johnston, C. A. Swenson, F. Borsa, A. V. Mahajan, L. L. Miller, T. Gu, A. I. Goldman, M. B. Maple, D. A. Gajewski, E. J. Freeman, N. R. Dilley, R. P. Dickey, J. Merrin, K. Kojima, G. M. Luke, Y. J. Uemura, O. Chmaissem, and J. D. Jorgensen, *LiV₂O₄: A heavy fermion transition metal oxide*, *Phys. Rev. Lett.* **78**, 3729 (1997).
- [S2] D. R. Hamann, Optimized norm-conserving Vanderbilt pseudopotentials, *Phys. Rev. B* **88**, 085117 (2013).
- [S3] M. van Setten, M. Giantomassi, E. Bousquet, M. Verstraete, D. Hamann, X. Gonze, and G.-M. Rignanese, The PseudoDojo: Training and grading a 85 element optimized norm-conserving pseudopotential table, *Computer Physics Communications* **226**, 39 (2018).
- [S4] A. A. Mostofi, J. R. Yates, G. Pizzi, Y.-S. Lee, I. Souza, D. Vanderbilt, and N. Marzari, An updated version of wannier90: A tool for obtaining maximally-localised Wannier functions, *Computer Physics Communications* **185**, 2309 (2014).
- [S5] F. Aryasetiawan, M. Imada, A. Georges, G. Kotliar, S. Biermann, and A. I. Lichtenstein, Frequency-dependent local interactions and low-energy effective models from electronic structure calculations, *Phys. Rev. B* **70**, 1 (2004).
- [S6] K. Nakamura, Y. Yoshimoto, Y. Nomura, T. Tadano, M. Kawamura, T. Kosugi, K. Yoshimi, T. Misawa, and Y. Motoyama, RESPACK: An ab initio tool for derivation of effective low-energy model of material, *Computer Physics Communications* **261**, 107781 (2021).
- [S7] E. Şaşıoğlu, C. Friedrich, and S. Blügel, Effective Coulomb interaction in transition metals from constrained random-phase approximation, *Phys. Rev. B* **83**, 121101 (2011).
- [S8] O. Parcollet, M. Ferrero, T. Ayril, H. Hafermann, I. Krivenko, L. Messio, and P. Seth, TRIQS: A toolbox for research on interacting quantum systems, *Computer Physics Communications* **196**, 398 (2015).
- [S9] M. Aichhorn, L. Pourovskii, P. Seth, V. Vildosola, M. Zingl, O. E. Peil, X. Deng, J. Mravlje, G. J. Kraberger, C. Martins, M. Ferrero, and O. Parcollet, TRIQS/DFTTools: A TRIQS application for ab initio calculations of correlated materials, *Computer Physics Communications* **204**, 200 (2016).
- [S10] P. Seth, I. Krivenko, M. Ferrero, and O. Parcollet, TRIQS/CTHYB: A continuous-time quantum Monte Carlo hybridisation expansion solver for quantum impurity problems, *Computer Physics Communications* **200**, 274 (2016).
- [S11] M. E. Merkel, A. Carta, S. Beck, and A. Hampel, solid.dmf: gray-boxing DFT+DMFT materials simulations with TRIQS, *Journal of Open Source Software* **7**, 4623 (2022).
- [S12] H. LaBollita, J. Kaye, and A. Hampel, Stabilizing the calculation of the self-energy in dynamical mean-field theory using constrained residual minimization (2023), [arXiv:2310.01266 \[cond-mat.str-el\]](https://arxiv.org/abs/2310.01266).
- [S13] F. A. Wolf, A. Go, I. P. McCulloch, A. J. Millis, and U. Schollwöck, Imaginary-time matrix product state impurity solver for dynamical mean-field theory, *Phys. Rev. X* **5**, 041032 (2015).
- [S14] J. Karp, M. Bramberger, M. Grundner, U. Schollwöck, A. J. Millis, and M. Zingl, Sr₂MoO₄ and Sr₂RuO₄: Disentangling the roles of Hund’s and van Hove physics, *Phys. Rev. Lett.* **125**, 166401 (2020).
- [S15] C. Hubig, F. Lachenmaier, N.-O. Linden, T. Reinhard, L. Stenzel, A. Swoboda, M. Grundner, and S. Mazdazad, *The SYTEN toolkit*.
- [S16] M. Caffarel and W. Krauth, Exact diagonalization approach to correlated fermions in infinite dimensions: Mott transition and superconductivity, *Phys. Rev. Lett.* **72**, 1545 (1994).
- [S17] N.-O. Linden, M. Zingl, C. Hubig, O. Parcollet, and U. Schollwöck, Imaginary-time matrix product state impurity solver in a real material calculation: Spin-orbit coupling in Sr₂RuO₄, *Phys. Rev. B* **101**, 041101 (2020).
- [S18] F. Verstraete, J. J. García-Ripoll, and J. I. Cirac, Matrix product density operators: Simulation of finite-temperature and dissipative systems, *Phys. Rev. Lett.* **93**, 207204 (2004).
- [S19] U. Schollwöck, The density-matrix renormalization group in the age of matrix product states, *Annals of Physics* **326**, 96 (2011), January 2011 Special Issue.

- [S20] S. Paeckel, T. Köhler, A. Swoboda, S. R. Manmana, U. Schollwöck, and C. Hubig, Time-evolution methods for matrix-product states, *Annals of Physics* **411**, 167998 (2019).
- [S21] M. Yang and S. R. White, Time-dependent variational principle with ancillary Krylov subspace, *Physical Review B* **102**, 10.1103/physrevb.102.094315 (2020).
- [S22] J. Haegeman, J. I. Cirac, T. J. Osborne, I. Pižorn, H. Verschelde, and F. Verstraete, Time-dependent variational principle for quantum lattices, *Phys. Rev. Lett.* **107**, 070601 (2011).
- [S23] J. Haegeman, C. Lubich, I. Oseledets, B. Vandereycken, and F. Verstraete, Unifying time evolution and optimization with matrix product states, *Phys. Rev. B* **94**, 165116 (2016).
- [S24] M. Yang and S. R. White, [Time dependent variational principle with ancillary Krylov subspace](#) (2020).
- [S25] M. Grundner, T. Blatz, J. Sous, U. Schollwöck, and S. Paeckel, Cooper-paired bipolaronic superconductors (2023), [arXiv:2308.13427 \[cond-mat.supr-con\]](#).
- [S26] C. Bertrand, D. Bauernfeind, P. T. Dumitrescu, M. Maček, X. Waintal, and O. Parcollet, Quantum quasi Monte Carlo algorithm for out-of-equilibrium green functions at long times, *Phys. Rev. B* **103**, 155104 (2021).
- [S27] R. Bulla, A. C. Hewson, and T. Pruschke, Numerical renormalization group calculations for the self-energy of the impurity Anderson model, *Journal of Physics: Condensed Matter* **10**, 8365 (1998).
- [S28] R. Peters, T. Pruschke, and F. B. Anders, Numerical renormalization group approach to Green's functions for quantum impurity models, *Phys. Rev. B* **74**, 245114 (2006).
- [S29] A. Weichselbaum and J. von Delft, Sum-rule conserving spectral functions from the numerical renormalization group, *Phys. Rev. Lett.* **99**, 076402 (2007).
- [S30] S.-S. B. Lee, F. B. Kugler, and J. von Delft, Computing local multipoint correlators using the numerical renormalization group, *Phys. Rev. X* **11**, 041007 (2021).
- [S31] A. Weichselbaum, Non-abelian symmetries in tensor networks: A quantum symmetry space approach, *Ann. Phys.* **327**, 2972 (2012); Tensor networks and the numerical renormalization group, *Phys. Rev. B* **86**, 245124 (2012); X-symbols for non-abelian symmetries in tensor networks, *Phys. Rev. Research* **2**, 023385 (2020).
- [S32] R. Žitko and T. Pruschke, Energy resolution and discretization artifacts in the numerical renormalization group, *Phys. Rev. B* **79**, 085106 (2009).
- [S33] S.-S. B. Lee and A. Weichselbaum, Adaptive broadening to improve spectral resolution in the numerical renormalization group, *Phys. Rev. B* **94**, 235127 (2016).
- [S34] S.-S. B. Lee, J. von Delft, and A. Weichselbaum, Doublon-holon origin of the subpeaks at the Hubbard band edges, *Phys. Rev. Lett.* **119**, 236402 (2017).
- [S35] F. B. Kugler, Improved estimator for numerical renormalization group calculations of the self-energy, *Phys. Rev. B* **105**, 245132 (2022).
- [S36] A. K. Mitchell, M. R. Galpin, S. Wilson-Fletcher, D. E. Logan, and R. Bulla, Generalized Wilson chain for solving multichannel quantum impurity problems, *Phys. Rev. B* **89**, 121105 (2014).
- [S37] K. M. Stadler, A. K. Mitchell, J. von Delft, and A. Weichselbaum, Interleaved numerical renormalization group as an efficient multiband impurity solver, *Phys. Rev. B* **93**, 235101 (2016).
- [S38] F. B. Kugler, M. Zingl, H. U. R. Strand, S.-S. B. Lee, J. von Delft, and A. Georges, Strongly correlated materials from a numerical renormalization group perspective: How the Fermi-liquid state of Sr_2RuO_4 emerges, *Phys. Rev. Lett.* **124**, 016401 (2020).
- [S39] F. B. Kugler, C.-J. Kang, and G. Kotliar, [Low-energy perspective on two-orbital Hund metals and the case of \$\text{LaNiO}_2\$](#) (2024), [arXiv:2312.11457](#).
- [S40] C. Urano, M. Nohara, S. Kondo, F. Sakai, H. Takagi, T. Shiraki, and T. Okubo, LiV_2O_4 spinel as a heavy-mass Fermi liquid: Anomalous transport and role of geometrical frustration, *Phys. Rev. Lett.* **85**, 1052 (2000).
- [S41] Y. Shimizu, H. Takeda, M. Tanaka, M. Itoh, S. Niitaka, and H. Takagi, An orbital-selective spin liquid in a frustrated heavy fermion spinel LiV_2O_4 , *Nature Communications* **3**, 981 (2012).
- [S42] H. Okabe, M. Hiraishi, A. Koda, K. M. Kojima, S. Takeshita, I. Yamauchi, Y. Matsushita, Y. Kuramoto, and R. Kadono, Metallic spin-liquid-like behavior of LiV_2O_4 , *Phys. Rev. B* **99**, 041113 (2019).
- [S43] S. Kondo, C. Urano, Y. Kurihara, M. Nohara, and H. Takagi, From the geometrically frustrated antiferromagnets ZnV_2O_4 and ZnCr_2O_4 to the heavy-mass Fermi liquid LiV_2O_4 , in *Magnetic Excitations in Strongly Correlated Electrons*, Proceedings of the International Workshop on Magnetic Excitations in Strongly Correlated Electrons August 19-22, 1999 Hamamatsu, Japan, edited by M. Takigawa, K. Ueda, and Y. Ueda (J. Phys. Soc. Jpn. 69 Suppl. B., 2000) p. 139.